Coupling Ideality of Integrated Planar High-Q Microresonators

Martin H. P. Pfeiffer, Junqiu Liu, Michael Geiselmann, and Tobias J. Kippenberg[*]

École Polytechnique Fédérale de Lausanne (EPFL), CH-1015 Lausanne, Switzerland

Chip-scale optical microresonators with integrated planar optical waveguides are useful building blocks for linear, nonlinear, and quantum-optical photonic devices alike. Loss reduction through improving fabrication processes results in several integrated microresonator platforms attaining quality (Q) factors of several millions. Beyond the improvement of the quality factor, the ability to operate the microresonator with high coupling ideality in the overcoupled regime is of central importance. In this regime, the dominant source of loss constitutes the coupling to a single desired output channel, which is particularly important not only for quantum-optical applications such as the generation of squeezed light and correlated photon pairs but also for linear and nonlinear photonics. However, to date, the coupling ideality in integrated photonic microresonators is not well understood, in particular, design-dependent losses and their impact on the regime of high ideality. Here we investigate design-dependent parasitic losses described by the coupling ideality of the commonly employed microresonator design consisting of a microring-resonator waveguide side coupled to a straight bus waveguide, a system which is not properly described by the conventional input-output theory of open systems due to the presence of higher-order modes. By systematic characterization of multimode high-Q silicon nitride microresonator devices, we show that this design can suffer from low coupling ideality. By performing 3D simulations, we identify the coupling to higher-order bus waveguide modes as the dominant origin of parasitic losses which lead to the low coupling ideality. Using suitably designed bus waveguides, parasitic losses are mitigated with a nearly unity ideality and strong overcoupling (i.e., a ratio of external coupling to internal resonator loss rate > 9) are demonstrated. Moreover, we find that different resonator modes can exchange power through the coupler, which, therefore, constitutes a mechanism that induces modal coupling, a phenomenon known to distort resonator dispersion properties. Our results demonstrate the potential for significant performance improvements of integrated planar microresonators for applications in quantum optics and nonlinear photonics achievable by optimized coupler designs.

I. INTRODUCTION

Microresonator devices are ubiquitously used in integrated photonic circuits and enable applications that range from filters [1], sensors [2], modulators [3], to nonlinear applications [4,5] such as wavelength conversion [6,7] and Kerr frequency comb and soliton generation [8,9]. Moreover, quantum-optical experiments such as the generation of squeezed light [10] and correlated photon pairs [11] have also been implemented based on integrated microresonator devices. While most microresonator devices in integrated photonics are formed by single-mode waveguides [12,13], many recent photonic integrated circuits rely on multimode waveguides due to their lower losses [14,15], higher data capacity [16], improved device integration [17], and tailored dispersion properties, e.g., to attain anomalous group-velocity dispersion required for parametric frequency conversion [18,19]. In contrast to the well-established approach of the input-output formalism of a damped quantum system [20], which considers a single well-defined input and output channel, the presence of higher-order modes as output channels requires consideration.

Early research on ultrahigh-Q microresonators in other platforms led to the development of several adjustable evanescent coupling techniques based on prisms and tapered optical fibers [21–25]. To quantitatively describe the performance of these couplers with multiple output channels, the "coupling ideality" was defined for tapered fiber coupling to microspheres as the ratio of the power coupled from the resonator to the fundamental fiber mode divided by the total power coupled to all guided and nonguided fiber modes [25]. A high coupling ideality enables us to operate the resonator in the strongly overcoupled regime, where the output losses are dominated by the coupling to the single desired output channel. This regime is relevant, in particular, for quantum optics, e.g., to preserve quantum correlations of generated intracavity photon pairs [11] and squeezed states of light [10]. It is, thus, important to avoid degradation of coupling ideality in the presence of multiple output channels.

In the context of integrated planar microresonator devices, design rules [26,27] and optimized coupler

[*] tobias.kippenberg@epfl.ch

geometries [17,28,29] have been reported. However, comparatively little attention has been paid to their coupler performance, especially with regard to the multimode nature of waveguides. Only few reports of coupler-induced excess losses [30,31] have been published, and most integrated microresonator devices, single- or multimode, rely on the coupler design consisting of a simple side-coupled straight bus waveguide with a cross section identical to the resonator waveguide.

Here we present a comprehensive investigation of integrated planar high-Q silicon nitride (Si_3N_4) microresonator devices with several different coupler designs. Experimental resonance characterization with sufficiently large statistics and full 3D numerical simulations allow us to unambiguously reveal the detrimental effect of nonideal coupler designs, even in the presence of statistical fluctuations of resonator properties due to fabrication variations. The commonly employed coupler design using the bus waveguide of the same cross section as the resonator is found to exhibit parasitic losses due to the modal coupling to higher-order bus waveguide modes, which can severely limit the device performance. In contrast, in the design of the multimode resonator coupled to a single-mode bus waveguide, we observe nearly ideal coupler performance. Finally, our simulations show that coupling between different resonator modes can originate from the coupler. This provides insight into the origin of modal coupling in microresonators observed in the previous work [9,32], which leads to a distortion of resonator dispersion properties.

II. ANALYTICAL DESCRIPTION OF A MULTIMODE COUPLING SECTION

Typically, the evanescent coupling of light to a microresonator is described using coupled-mode theory as a power transfer to a resonator mode at the rate $\kappa_{ex,0}$ [23,24,33]. Treating the resonator in a lumped model [34,35], the coupling rate $\kappa_{ex,0}$ is typically estimated using the model of coupling between two copropagating modes in adjacent waveguides [36]. In contrast to the power coupling ratios of conventional directional couplers, the high-Q microresonator's low internal loss rate κ_0 requires only minute power transfer to achieve critical coupling (i.e., $\kappa_{ex,0} = \kappa_0$) for which the intracavity power buildup is maximal. Thus, the coupled modes in both the resonator and the bus waveguides can be essentially treated as independent, and $\kappa_{ex,0}$ depends on the mutual modal overlap and propagation constant mismatch $\Delta\beta$ (i.e., phase mismatch) [1,23,36]. This model is widely applied, as it provides a qualitative insight for most cases where coupling between only two modes is considered, neglecting the coupling to other modes.

In practice for high-Q microresonators, a commonly employed coupler design consists of a side-coupled straight bus waveguide identical in cross section to the resonator

waveguide. The cross section is chosen in order to match the propagation constants of, e.g., the fundamental resonator and bus waveguide modes. However, in the case of multimode waveguides, as found for tapered-fiber-coupled high-Q microspheres [25], coupling between different modes has to be considered, as depicted in Fig. 1(a). Moreover, the coupler can scatter light into free-space modes and recently was also identified to couple the counterpropagating clockwise and counterclockwise waveguide modes [31], which is not considered in the present work. As a result, the corresponding equations of motion for the resonator modal amplitude a_0 of frequency ω_0 in the rotating frame of the driving laser ω_L have to be extended to

$$\frac{d}{dt}a_0 = i\Delta_0 a_0 - \left(\frac{\kappa_0 + \kappa_{ex,0} + \kappa_p}{2}\right)a_0$$
$$+ \sqrt{\kappa_{ex,0}}s_{in} + \frac{i}{2}\sum_{n\neq0}\kappa_{0,n}a_n e^{i\Delta_n t}. \quad (1)$$

Here, $\Delta_0 = \omega_L - \omega_0$ and $\Delta_n = \omega_L - \omega_n$ are the frequency detunings between the driving laser with amplitude s_{in} and the resonator modes a_0 and a_n. The intracavity field decays due to the internal loss rate κ_0 and the external
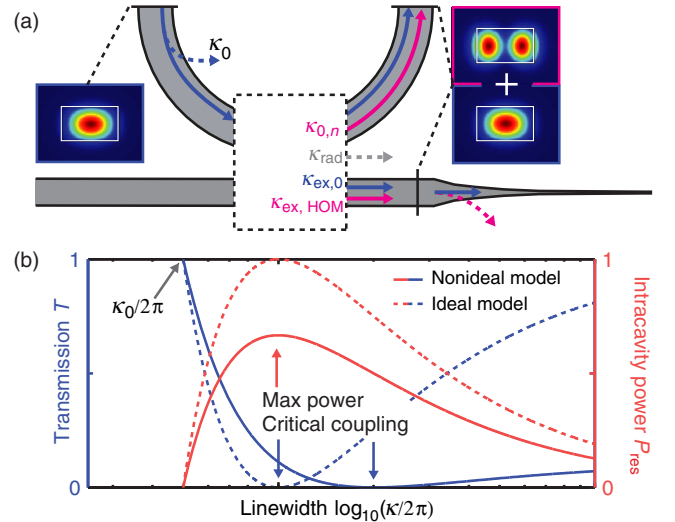

FIG. 1. (a) Schematic representation of the coupling rates in an integrated microresonator with multimode waveguides. The parasitic coupling processes of a fundamental resonator mode to higher-order bus waveguide modes are illustrated. κ_0 represents the resonator's internal loss rate, and $\kappa_{ex,0}$ represents the coupling rate to the fundamental bus waveguide mode. $\kappa_{ex,HOM}$ represents the coupling rate to the higher-order bus waveguide modes, which are later filtered out by the inverse taper mode converter. $\kappa_{0,n}$ represents the coupling rate to other resonator modes, while κ_{rad} represents the coupling rate to free-space modes. (b) Plot of the transmission T (blue) and the intracavity power P_{res} (red) as a function of the total linewidth $\kappa/2\pi$ for the ideal ($I = 1$, dashed lines) and nonideal ($I = 0.67$, solid lines) cases.

coupling rate $\kappa_{\mathrm{ex},0}$ to the fundamental bus waveguide mode. The radiation into free-space modes with the rate κ_{rad} and to higher-order bus waveguide modes with the rate $\kappa_{\mathrm{ex,HOM}} = \sum_{q\neq0}\kappa_{\mathrm{ex},q}$ are considered as parasitic coupling losses and, thus, form the parasitic coupling rate $\kappa_p = \kappa_{\mathrm{rad}} + \kappa_{\mathrm{ex,HOM}}$, which accelerates the intracavity field decay.

In addition, the modal coupling term $(i/2)\sum_{n\neq0}\kappa_{0,n}a_n e^{i\Delta_n t}$ is introduced to account for the fact that the resonator mode a_0 can couple to other modes with the rate $\kappa_{0,n}$. Such modal coupling is usually considered to arise from surface roughness but is later found to originate also from the coupler. This term is relevant only if the coupled modes are simultaneously resonant. Such modal coupling causes deviations of the resonance frequencies, so called avoided modal crossings, that locally distort the resonator dispersion. At such modal crossing points, the coupling to another resonator mode a_n (with total loss κ_n) effectively adds an extra contribution to the parasitic loss κ_p. However, away from the modal crossing point where only the resonator mode a_0 is resonant, the added parasitic loss is negligible. The coupling ideality I of the resonator mode a_0 describing the relative strength of parasitic coupling rates is defined according to Ref. [25] as

$$I = \frac{\kappa_{\mathrm{ex},0}}{\kappa_{\mathrm{ex},0} + \kappa_p}. \quad (2)$$

In the following, the effects of coupling ideality on device performance are considered. While the scattering of light into free-space modes directly represents a power loss, power coupled to higher-order modes of the bus waveguide is not necessarily lost. In most cases, however, the higher-order bus waveguide modes are filtered out, e.g., by inverse taper mode converters [37]. Thus, the measured power at the device facets consists only of the power of the bus waveguide's fundamental mode, and, therefore, the input-output relation $s_{\mathrm{out}} = s_{\mathrm{in}} - \sqrt{\kappa_{\mathrm{ex},0}}a_0$ holds, and $\kappa_{\mathrm{ex,HOM}}$ represents a parasitic loss which enlarges the resonance linewidth. On resonance ($\Delta_0 = 0$), the device power transmission T and intracavity power P_{res} as a function of the coupling ideality I and coupling parameter $K = \kappa_{\mathrm{ex},0}/\kappa_0$ are expressed as

$$T = \left|1 - \frac{2}{K^{-1} + I^{-1}}\right|^2, \quad (3)$$

$$P_{\mathrm{res}} = \frac{D_1}{2\pi}\frac{4}{\kappa_{\mathrm{ex},0}(K^{-1} + I^{-1})^2}P_{\mathrm{in}}. \quad (4)$$

Here, $D_1/2\pi$ is the resonator free spectral range (FSR). Assuming an input power $P_{\mathrm{in}} = |s_{\mathrm{in}}|^2 = 1$ and a constant D_1, Fig. 1(b) plots both the transmission T and intracavity power P_{res} as a function of the total linewidth $\kappa/2\pi = (\kappa_0 + \kappa_{\mathrm{ex},0}/I)/2\pi$ for the ideal ($I = 1$) and nonideal ($I < 1$)

cases, with a constant κ_0 and varying $\kappa_{\mathrm{ex},0}$. The effects of the nonideal coupling become apparent: in the case of the ideal coupling (dashed lines), the point of the full power extinction (i.e., $T = 0$, the critical coupling point) coincides with the point of the maximum intracavity power. This relation is different for the nonideal case (solid lines), in which the parasitic losses increase linearly with the coupling rate $\kappa_p = 0.5\kappa_{\mathrm{ex},0}$ in a first-order approximation. More important, the value of the maximum intracavity power is reduced compared to the ideal case. Because of the parasitic losses, critical coupling and overcoupling are achieved only at larger total resonator linewidth, or they cannot be achieved at all if $\kappa_p > \kappa_{\mathrm{ex},0}$. It is, therefore, evident that in applications exploiting the resonator's power enhancement, e.g., for nonlinear photonics, device performance will improve with higher coupling ideality. Likewise, the analysis shows that linewidth measurements carried out at the critical coupling point include possible parasitic loss channels preventing faithful measurements of the intrinsic quality factor.

III. EXPERIMENTAL STUDY OF COUPLING IDEALITY

We experimentally study the coupling ideality for integrated Si_3N_4 microresonators, a widely employed platform for on-chip nonlinear photonics such as Kerr frequency comb generation [8] and quantum optical experiments [10,11,38]. For microresonator platforms with adjustable couplers, e.g., tapered fibers and prism couplers, changing the evanescent coupling rates allows us to measure the transmission-linewidth dependence of a single resonance [23,25] and to retrieve the coupling ideality via Eq. (3). In contrast, here we study photonic chips with several microresonator devices that consist of resonator and bus waveguides, as well as inverse taper mode converters [37] placed at the chip facets. The microresonator devices on each chip are identical but have varying distances between the resonator and bus waveguide providing different coupling rates. In this case, coupling ideality is evaluated by analyzing the transmission-linewidth dependence of many resonances acquired for each microresonator device. By measuring several resonators with varying gap distances, we overcome the variations in quality factor Q inherent to the fabrication process itself.

The waveguide core is made from silicon nitride (Si_3N_4) and fully cladded with silicon dioxide (SiO_2). All measured samples are fabricated on the same wafer using a photonic Damascene process [39]. In contrast to typical subtractive processes, this process allows for void-free high-aspect-ratio coupler gap fabrication, eliminating excess losses due to the presence of voids. By using lensed fibers, light is coupled efficiently (loss < 3 dB per facet) into a single fundamental mode of the bus waveguide. Calibrated transmission traces are acquired for all devices on the chip from 1500 to 1630 nm with a similar method as described in Ref. [40]. A polarization controller is used to select and

maintain a stable input polarization over the full measurement bandwidth. Resonances in each recorded device transmission trace are automatically identified and fitted using a model of a split Lorentzian line shape [41]. The resonances are grouped into different mode families by measuring their mutual FSRs and comparing them to finite-element simulations of the device geometry.

Figure 2 compares the measured transmission-linewidth dependence of the resonator's transverse-magnetic fundamental mode families ($TM_{R,00}$) for two 1-THz FSR [Figs. 2(a) and 2(c)] and two 100-GHz FSR [Figs. 2(b) and 2(d)] microresonator device chips. The cross section of the resonator waveguide is 0.87 μm in height, and 2 μm (100-GHz FSR) and 1.5 μm (1-THz FSR) in width, respectively. Each point represents a measured resonance, and the points with the same color are from the same microresonator device. Different colors denote microresonator devices with different resonator-bus distances. The red dashed line traces out the transmission-linewidth dependence for the ideal coupling of unity ideality with a fixed internal loss κ_0.

Figure 2(a) shows an example of low coupling ideality: a small radius ($r \approx 23$ μm), 1-THz FSR resonator coupled to a multimode bus waveguide of the same cross section. The measured resonances of the fundamental $TM_{R,00}$ mode family have gigahertz linewidth and low extinction (i.e., high transmission), and their measured transmission-linewidth dependence does not follow a clear trend. Because of the identical cross sections of the resonator and the bus waveguides, this coupler design can be naively assumed to provide a good propagation constant match between the resonator and bus waveguide TM fundamental modes, i.e., $TM_{R,00}$ and $TM_{B,00}$. However, due to the small ring radius $r \approx 23$ μm, the propagation constants of the $TM_{R,00}$ and $TM_{B,00}$ modes are strongly mismatched, despite the identical waveguide cross sections.

As shown in Fig. 2(b), a 100-GHz FSR resonator with a 10 times larger radius ($r \approx 230$ μm) can also have limited coupling ideality when interfaced with a straight waveguide of the same cross section. Although featuring resonance linewidths below $\kappa_0/2\pi = 30$ MHz and an average linewidth of $\kappa_0/2\pi \approx 50$ MHz, the microresonator cannot be efficiently overcoupled, indicating the presence of parasitic losses.

Figures 2(c) and 2(d) present two possible coupler designs that improve coupling ideality. First, as shown in Fig. 2(c), almost unity ideality and strong overcoupling are achieved for a 1-THz FSR microresonator coupled to a single-mode bus waveguide. The bus waveguide has a cross section of 0.6 μm height and 0.4 μm width due to the aspect-ratio-dependent etch rate during the preform etch [39]. It can, thus, be concluded that the main source of parasitic losses leading to the low ideality in Fig. 2(a) originates from the coupling to higher-order bus waveguide modes. Therefore, using a single-mode bus waveguide can essentially avoid this kind of parasitic loss and significantly improve coupling ideality to near unity. As a result, strong overcoupling can be achieved with an external coupling rate $\kappa_{ex,0}$ almost a magnitude larger than the internal losses (coupling parameter $K = \kappa_{ex,0}/\kappa_0 = \kappa/\kappa_0 - 1 > 9$).

However, in most cases, when using a single-mode bus waveguide, though coupling ideality improves, the propagation constants of the bus and resonator fundamental
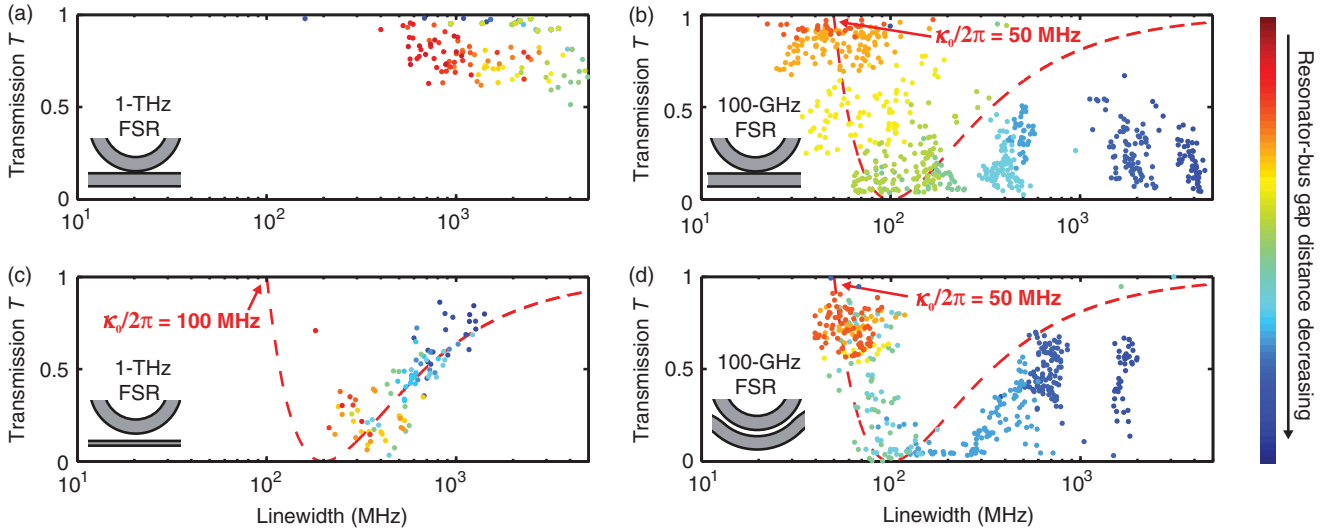

FIG. 2. Characterization of coupling ideality for the fundamental $TM_{R,00}$ mode family of 1-THz FSR [panels (a),(c)] and 100-GHz FSR [panels (b),(d)] microresonator devices. Dots of the same color correspond to resonances of the same resonator with the color bar indicating their mutual resonator-bus distance trend. The red dashed lines indicate the trend expected for ideal coupling to resonators with the internal loss rates of $\kappa_0/2\pi = 100$ MHz (c) and $\kappa_0/2\pi = 50$ MHz (b),(d). For (a), (b), and (d), the bus waveguide has the same cross section as the resonator waveguide. Panels (b) and (d) show improved ideality and achieved overcoupling through the use of a single-mode bus waveguide (b) and a pulley-style coupler (d).

modes (e.g., $TM_{B,00}$ and $TM_{R,00}$) are strongly mismatched, which limits the maximum value of the coupling rate $\kappa_{ex,0}$. Thus, a narrow gap is needed to achieve sufficient modal overlap and a large enough coupling rate $\kappa_{ex,0}$ to achieve overcoupling. For the 1-THz FSR resonator, a coupling rate $\kappa_{ex,0}$ sufficient for overcoupling is achieved due to its small mode volume and low internal loss per round-trip ($\propto \kappa_0/D_1$). However, for smaller FSR resonators with larger mode volumes, e.g., 100-GHz FSR, overcoupling might not be achieved in the case of strong propagation constant mismatch, as fabrication processes pose limitations on the narrowest resonator-bus distance. One alternative solution for smaller FSR, larger radius resonators to achieve efficient overcoupling is to use a pulley-style coupler [27]. Figure 2(d) shows the measurement results for 100-GHz FSR micro-resonators coupled with a multimode bus waveguide of the same cross section as the resonator but in a pulley-style configuration. The comparison between the two 100-GHz FSR resonators in Figs. 2(b) and 2(d) reveals an improved coupling ideality for the pulley-style coupler. The improved coupling ideality of the pulley-style coupler is not as high as in the case of the 1-THz FSR resonator coupled to a single-mode bus waveguide in Fig. 2(c). However, such a comparison neglects the large difference in mode volume. In fact, the fundamental $TM_{R,00}$ mode of the present 100-GHz FSR resonator cannot be overcoupled using a single-mode bus waveguide, as the strong propagation constant mismatch limits the achievable coupling rates.

IV. SIMULATIONS OF COUPLING IDEALITY

In order to verify the dominant origin of parasitic losses and the observed strong design dependence of coupling ideality, we implement full 3D finite-difference time-domain (FDTD) simulations [42] (*Lumerical FDTD Solutions*). This allows us to study numerically the light propagation through the coupler by solving Maxwell's equations in the time domain. The simulation model is shown in Fig. 3(a). Considering the designs of the micro-resonator devices experimentally characterized in the previous section, the resonator and the bus waveguide have the same cross sections, which is 1.5×0.87 μm^2 (width× height) for the 1-THz FSR resonator and 2.0×0.87 μm^2 for the 100-GHz FSR resonator. The sidewall angle is $\alpha = 90°$, and the resonator-bus gap distance is set as 0.5 μm. A graded mesh of rectangular cells with the maximum cell volume of $(22 \text{ nm})^3$ is applied to the simulation region. The boundary condition enclosing the full simulation region is set as a perfectly matched layer (PML) [43] to absorb the incident light to the boundary and, thus, to prevent backreflection.

The resonator fundamental $TM_{R,00}$ mode at the center wavelength of 1550 nm is launched with unity power, and the light field propagates until the field distribution reaches the stationary state in the full simulation region. Monitors
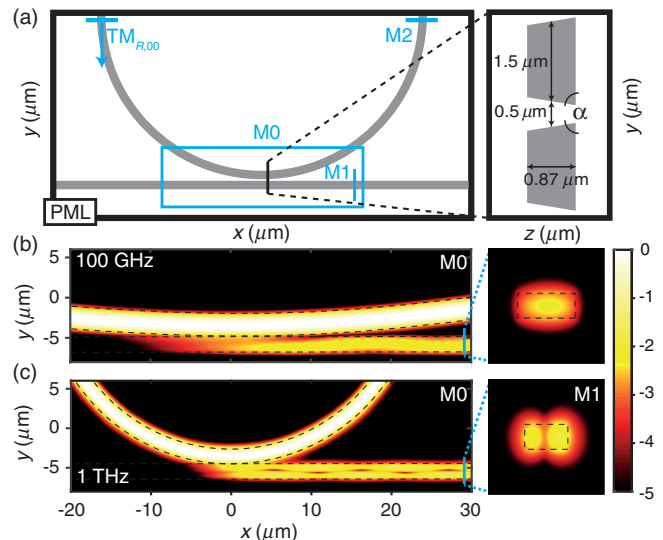

FIG. 3. FDTD simulations of waveguide coupling for 100-GHz and 1-THz FSR resonators. (a) Schematic representation of the simulation model. The resonator and the bus waveguide (both in gray) have the same cross sections (2.0×0.87 μm^2 for 100-GHz FSR and 1.5×0.87 μm^2 for 1-THz FSR), the sidewall angle $\alpha = 90°$, and are separated by a 0.5-μm gap. The boundary condition (thick black lines) enclosing the simulation region is set as a PML. The resonator fundamental $TM_{R,00}$ mode is launched into the resonator waveguide and the monitors M0, M1, and M2 record the field distributions in their individual planes. (b),(c) The field distributions recorded by M0 and M1 for the 100-GHz and 1-THz FSR resonators. The $TM_{R,00}$ mode is coupled not only to the bus waveguide's fundamental $TM_{B,00}$ mode but also to its higher-order $TM_{B,10}$ mode. The propagation constant difference of both bus waveguide modes causes the interference pattern visible along their propagation direction. This interference pattern indicates degraded coupling ideality, which is more prominent in the case of 1-THz FSR. The color bar denotes the field intensity in logarithmic scale.

M0, M1, and M2 record the field distributions in their individual monitor planes. Figures 3(b) and 3(c) show the field distributions recorded by M0 and M1 for the resonators of 100-GHz and 1-THz FSR, respectively. An interference pattern in the field distribution along the bus waveguide is observed in both cases and is more prominent in the case of 1-THz FSR. The field distributions recorded by M1 show that (i) in the case of 100-GHz FSR, the field propagates predominantly in the bus waveguide fundamental $TM_{B,00}$ mode, which indicates a limited nonunity coupling ideality, (ii) while in the case of 1-THz FSR, a significant portion of power is coupled to the higher-order $TM_{B,10}$ mode that beats with the $TM_{B,00}$ mode along the propagation in the bus waveguide, which indicates a lower coupling ideality. These qualitative conclusions from Fig. 3 agree well with the experimental observation that the 1-THz FSR resonator in Fig. 2(a) shows higher parasitic losses, and, thus, a lower coupling ideality compared to the 100-GHz FSR resonator in Fig. 2(b).

We perform further analysis to quantify the degradation of coupling ideality in the 1-THz FSR resonators. The total power P(total) coupled into the bus waveguide can be obtained by calculating the Poynting vector normal to the monitor plane of M1. In addition, using the "mode expansion function" of *Lumerical FDTD Solutions*, the field distribution recorded by M1 can be projected on each waveguide eigenmode, and their individual power ($>10^{-12}$) can be calculated. All powers are normalized as they derive from the resonator fundamental $TM_{R,00}$ mode that is launched with unity power. The respective coupling rates $\kappa_{ex,i}$ follow by relating the coupled power to the resonator FSR ($D_1/2\pi$) by $\kappa_{ex,i} = D_1 \times P(i)$. The fundamental bus waveguide mode's power $P(TM_{B,00})$ can be obtained, and the coupling ideality can, thus, be approximately estimated as $I = P(TM_{B,00})/P(total)$, assuming that the coupling to the higher-order bus waveguide modes ($\kappa_{ex,HOM}$) is the dominant origin of parasitic losses. In addition, in order to investigate how the resonator mode is affected by the coupler, the field distribution recorded by M2 in the resonator waveguide after the coupling section is also decomposed into individual modes.

Table I compiles the simulation results of different coupler designs (nos. 1–7) with varying geometrical parameters, including the resonator FSR, the cross sections of the resonator and the bus waveguides, the gap distance, and the waveguide sidewall angle α. This angle α takes into account the fact that the fabricated waveguides have slanted sidewalls ($\alpha \approx 80°$). For each design, we calculate the individual power of the selected eigenmodes in the resonator ($TM_{R,10}$ and transverse-electric fundamental resonator mode $TE_{R,00}$) and the bus waveguide ($TM_{B,00}$, $TM_{B,10}$, and $TE_{B,00}$), and numerically compute the coupling ideality I.

First, Table I shows that the commonly employed coupler design of a straight bus waveguide coupling to a resonator waveguide of the same cross section has a higher coupling ideality for the 100-GHz FSR resonators (no. 7, $I \approx 0.968$) than for the 1-THz FSR resonators (no. 2, $I \approx 0.163$). This agrees well with the previously discussed observations in Figs. 2 and 3. The degraded ideality in the case of the 1-THz FSR resonators illustrates the limited applicability of this coupler design. The fact that the resonator radius strongly affects coupling ideality is more directly seen by comparing the cases no. 2 and 6, as both cases have exactly the same geometrical parameters except for the resonator FSR.

In addition, the coupling ideality of 100-GHz FSR resonators (nos. 6 and 7) depends also on the waveguide width when coupled to a bus waveguide of the same cross section. The degradation of coupling ideality in case no. 7 is due to more power coupled to the higher-order bus waveguide mode ($TM_{B,10}$), which can be explained with the smaller propagation constant mismatch between the fundamental resonator mode ($TM_{R,00}$) and the higher-order bus waveguide mode ($TM_{B,10}$). Additionally, the wider waveguide cross section reduces the mutual modal overlap between the fundamental $TM_{R,00}$ and $TM_{B,00}$ modes and, thus, their mutual power transfer $P(TM_{B,00})$. Furthermore, our simulations verify the experimentally observed improvement of coupling ideality for the 1-THz FSR resonator coupled to a single-mode bus waveguide (no. 5, $I \approx 1.00$). However, this is achieved at the expense of reducing power transfer to the bus waveguide $P(TM_{B,00})$ by nearly 1 order of magnitude, which is due to the propagation constant mismatch between the $TM_{B,00}$ and $TM_{R,00}$ modes.

TABLE I. Table of simulated coupled powers for different coupler designs. The resonator fundamental $TM_{R,00}$ mode is launched with unity power. The individual modal powers in the resonator and the bus waveguides after the coupling section are listed. For every simulated case, the resonator FSR, the cross section of the resonator and the bus waveguides, the gap distance, and the sidewall angle are listed. P(total) is the total power recorded in the bus waveguide after the coupling section, and I is the coupling ideality calculated as $I = P(TM_{B,00})/P(total)$. The bus waveguide is single mode (SM) in case no. 5, while all the other bus waveguides are multimode. Modes which do not exist are marked with three center dots "($\cdots$)."

No.	1	2	3	4	5	6	7
FSR	1 THz	1 THz	1 THz	1 THz	1 THz	100 GHz	100 GHz
$w_{res} \times h_{res}$ (μm^2)	1.5×0.87	1.5×0.87	1.5×0.87	1.5×0.87	1.5×0.87	1.5×0.87	2.0×0.87
$w_{bus} \times h_{bus}$ (μm^2)	($\cdots$)	1.5×0.87	1.5×0.87	1.5×0.87	0.40×0.60 (SM)	1.5×0.87	2.0×0.87
Gap (μm)	($\cdots$)	0.5	0.2	0.5	0.5	0.5	0.5
α	90°	90°	90°	80°	90°	90°	90°
$P(TM_{R,10})$	1.28×10^{-4}	7.87×10^{-4}	0.0116	7.6×10^{-4}	3.9×10^{-4}	1.82×10^{-6}	1.72×10^{-5}
$P(TE_{R,00})$	$<10^{-12}$	$<10^{-12}$	$<10^{-12}$	1.08×10^{-6}	$<10^{-12}$	$<10^{-12}$	$<10^{-12}$
$P(TM_{B,00})$	$\cdots$	3.36×10^{-3}	0.0344	3.31×10^{-3}	3.92×10^{-4}	0.0237	5.73×10^{-3}
$P(TM_{B,10})$	($\cdots$)	0.0176	0.0974	0.0173	($\cdots$)	3.4×10^{-6}	1.81×10^{-4}
$P(TE_{B,00})$	$\cdots$	$<10^{-12}$	$<10^{-12}$	4.89×10^{-6}	$<10^{-12}$	$<10^{-12}$	$<10^{-12}$
P(total)	($\cdots$)	0.0209	0.133	0.0203	3.92×10^{-4}	0.0237	5.92×10^{-3}
I	($\cdots$)	0.161	0.259	0.161	1.00	1.00	0.968

Second, though only the fundamental $TM_{R,00}$ mode is launched in the resonator, a nonzero power in a higher-order mode [$P(TM_{R,10})$] is recorded by M2. In addition, it is observed by comparing the uncoupled (no. 1) and coupled cases (nos. 2 and 3) that this power in the higher-order resonator-mode power $P(TM_{R,10})$ increases with decreasing gap distance. In the case of the uncoupled resonator (no. 1), the appearance of $P(TM_{R,10}) = 1.28 \times 10^{-4}$ is mainly attributed to the mesh, which acts as a $(22\text{-nm})^3$ surface roughness at the material interface. Such surface roughness is well known to lead to modal coupling, e.g., the coupling between the resonator modes $TM_{R,00}$ and $TM_{R,10}$. In addition, compared with the 100-GHz FSR resonator (nos. 6 and 7), this effect is more prominent in the 1-THz FSR resonator (no. 1). Nevertheless, for the coupled resonators (nos. 2 and 3), the enhancement of $P(TM_{R,10})$ with decreasing gap distance unambiguously reveals the existence of a coupler-induced modal coupling. This is an important finding revealing an origin of modal coupling [32] in microresonators, which causes distortion of microresonator dispersion properties.

Third, the coupling of the launched $TM_{R,00}$ mode to the modes with the orthogonal polarization, i.e., $TE_{R,00}$ in the resonator and $TE_{B,00}$ in the bus waveguide, is observed in the case of slanted waveguide sidewalls (no. 4). Such a cross-polarization coupling occurs if the modal field distribution is asymmetric with respect to its center [44,45], and its strength depends on the degree of this asymmetry. In the simulated case, the asymmetry is introduced by the ring bending and the $\alpha = 80°$ sidewall angle. However, by comparing cases no. 2 and 4, the sidewall angle $\alpha = 80°$ enhances only the power $P(TE_{R,00})$ significantly, while the powers of other modes as well as the coupling ideality remain almost the same.

V. CONCLUSION

In summary, we present a study of coupling ideality of monolithically integrated high-Q Si_3N_4 microresonator devices. For the commonly employed coupler design where both the resonator and the bus waveguides have the same cross sections, we reveal the presence of parasitic losses due to the coupling to higher-order bus waveguide modes. This coupling degrades the coupling ideality, which is shown both through systematic experimental characterization of resonances and full 3D FDTD simulations. Consequently, an optimized coupler design using a single-mode bus waveguide with efficiently mitigated parasitic losses (ideality $I \approx 1$) and achieved strong overcoupling ($K > 9$) is demonstrated. Moreover, we discover that the coupler waveguide can induce modal coupling between different resonator modes, which is frequently observed in high-Q microresonators.

For microresonator devices based on multimode waveguides, coupling ideality is nontrivial to analyze and strongly depends on coupler designs and mode families. State-of-the-art microresonator devices for applications typically operate around the critical coupling point or the overcoupled regime; thus, high device performance requires optimized coupler designs with low parasitic losses and high coupling ideality. Our study not only reveals the design-dependent coupling ideality for integrated microresonator devices but also demonstrates the importance of anticipating coupling ideality in device design and the significant improvements it can unlock. The ability to strongly overcouple planar integrated photonic resonators will, in particular, benefit quantum-optical and nonlinear photonic experiments.

[1] B. E. Little, S. T. Chu, H. A. Haus, J. Foresi, and J. Laine, Microring resonator channel dropping filters, J. Lightwave Technol. 15, 998 (1997).

[2] K. De Vos, I. Bartolozzi, E. Schacht, P. Bienstman, and R. Baets, Silicon-on-insulator microring resonator for sensitive and label-free biosensing, Opt. Express 15, 7610 (2007).

[3] G. T. Reed, G. Mashanovich, F. Y. Gardes, and D. J. Thomson, Silicon optical modulators, Nat. Photonics 4, 518 (2010).

[4] J. Leuthold, C. Koos, and W. Freude, Nonlinear silicon photonics, Nat. Photonics 4, 535 (2010).

[5] D. J. Moss, R. Morandotti, A. L. Gaeta, and M. Lipson, New CMOS-compatible platforms based on silicon nitride and hydex for nonlinear optics, Nat. Photonics 7, 597 (2013).

[6] Q. Li, M. Davanço, and K. Srinivasan, Efficient and low-noise single-photon-level frequency conversion interfaces using silicon nanophotonics, Nat. Photonics 10, 406 (2016).

[7] X. Guo, C.-L. Zou, H. Jung, and H. X. Tang, On-Chip Strong Coupling and Efficient Frequency Conversion between Telecom and Visible Optical Modes, Phys. Rev. Lett. 117, 123902 (2016).

[8] T. J. Kippenberg, R. Holzwarth, and S. A. Diddams, Microresonator-based optical frequency combs, Science 332, 555 (2011).

[9] V. Brasch, M. Geiselmann, T. Herr, G. Lihachev, M. H. P. Pfeiffer, M. L. Gorodetsky, and T. J. Kippenberg, Photonic chipbased optical frequency comb using soliton Cherenkov radiation, Science 351, 357 (2016).

[10] A. Dutt, K. Luke, S. Manipatruni, A. L. Gaeta, P. Nussenzveig, and M. Lipson, On-Chip Optical Squeezing, Phys. Rev. Applied **3**, 044005 (2015).

[11] C. Reimer, M. Kues, P. Roztocki, B. Wetzel, F. Grazioso, B. E. Little, S. T. Chu, T. Johnston, Y. Bromberg, L. Caspani, D. J. Moss, and R. Morandotti, Generation of multiphoton entangled quantum states by means of integrated frequency combs, Science **351**, 1176 (2016).

[12] B. Jalali and S. Fathpour, Silicon photonics, J. Lightwave Technol. **24**, 4600 (2006).

[13] R. Nagarajan *et al.*, Large-scale photonic integrated circuits, IEEE J. Sel. Top. Quantum Electron. **11**, 50 (2005).

[14] M. Cherchi, S. Ylinen, M. Harjanne, M. Kapulainen, and T. Aalto, Dramatic size reduction of waveguide bends on a micron-scale silicon photonic platform, Opt. Express **21**, 17814 (2013).

[15] J. F. Bauters, M. J. R. Heck, D. D. John, J. S. Barton, C. M. Bruinink, A. Leinse, R. G. Heideman, D. J. Blumenthal, and J. E. Bowers, Planar waveguides with less than 0.1 dB/m propagation loss fabricated with wafer bonding, Opt. Express **19**, 24090 (2011).

[16] L.-W. Luo, N. Ophir, C. P. Chen, L. H. Gabrielli, C. B. Poitras, K. Bergmen, and M. Lipson, WDM-compatible mode-division multiplexing on a silicon chip, Nat. Commun. **5**, 3069 (2014).

[17] M. T. Wade, J. M. Shainline, J. S. Orcutt, R. J. Ram, V. Stojanovic, and M. A. Popovic, Spoked-ring microcavities: Enabling seamless integration of nanophotonics in unmodified advanced CMOS microelectronics chips, Proc. SPIE Int. Soc. Opt. Eng. **8991**, 89910B (2014).

[18] A. C. Turner, C. Manolatou, B. S. Schmidt, M. Lipson, M. A. Foster, J. E. Sharping, and A. L. Gaeta, Tailored anomalous group-velocity dispersion in silicon channel waveguides, Opt. Express **14**, 4357 (2006).

[19] J. Riemensberger, K. Hartinger, T. Herr, V. Brasch, R. Holzwarth, and T. J. Kippenberg, Dispersion engineering of thick high-Q silicon nitride ring-resonators via atomic layer deposition, Opt. Express **20**, 27661 (2012).

[20] C. W. Gardiner and M. J. Collett, Input and output in damped quantum systems: Quantum stochastic differential equations and the master equation, Phys. Rev. A **31**, 3761 (1985).

[21] V. B. Braginsky, M. L. Gorodetsky, and V. S. Ilchenko, Quality-factor and nonlinear properties of optical whispering-gallery modes, Phys. Lett. A **137**, 393 (1989).

[22] J. C. Knight, G. Cheung, F. Jacques, and T. A. Birks, Phase-matched excitation of whispering-gallery-mode resonances by a fiber taper, Opt. Lett. **22**, 1129 (1997).

[23] M. L. Gorodetsky and V. S. Ilchenko, Optical microsphere resonators: Optimal coupling to high-Q whispering gallery modes, J. Opt. Soc. Am. B **16**, 147 (1999).

[24] M. Cai, O. Painter, and K. J. Vahala, Observation of Critical Coupling in a Fiber Taper to a Silica-Microsphere Whispering-Gallery Mode System, Phys. Rev. Lett. **85**, 74 (2000).

[25] S. M. Spillane, T. J. Kippenberg, O. J. Painter, and K. J. Vahala, Ideality in a Fiber-Taper-Coupled Microresonator System for Application to Cavity Quantum Electrodynamics, Phys. Rev. Lett. **91**, 043902 (2003).

[26] M. Soltani, S. Yegnanarayanan, and A. Adibi, Ultra-high Q planar silicon microdisk resonators for chip-scale silicon photonics, Opt. Express **15**, 4694 (2007).

[27] E. S. Hosseini, S. Yegnanarayanan, A. H. Atabaki, M. Soltani, and A. Adibi, Systematic design and fabrication of high-Q single-mode pulley-coupled planar silicon nitride microdisk resonators at visible wavelengths, Opt. Express **18**, 2127 (2010).

[28] M. Ghulinyan, F. Ramiro-Manzano, N. Prtljaga, R. Guider, I. Carusotto, A. Pitanti, G. Pucker, and L. Pavesi, Oscillatory Vertical Coupling between a Whispering-Gallery Resonator and a Bus Waveguide, Phys. Rev. Lett. **110**, 163901 (2013).

[29] D. T. Spencer, J. F. Bauters, M. J. R. Heck, and J. E. Bowers, Integrated waveguide coupled Si_3N_4 resonators in the ultrahigh-Q regime, Optica **1**, 153 (2014).

[30] F. Xia, L. Sekaric, and Y. A. Vlasov, Mode conversion losses in silicon-on-insulator photonic wire based racetrack resonators, Opt. Express **14**, 3872 (2006).

[31] A. Li, T. Van Vaerenbergh, P. De Heyn, P. Bienstman, and W. Bogaerts, Backscattering in silicon microring resonators: A quantitative analysis, Laser Photonics Rev. **431**, 420 (2016).

[32] T. Herr, V. Brasch, J. D. Jost, I. Mirgorodskiy, G. Lihachev, M. L. Gorodetsky, and T. J. Kippenberg, Mode Spectrum and Temporal Soliton Formation in Optical Microresonators, Phys. Rev. Lett. **113**, 123901 (2014).

[33] H. A. Haus, *Waves and Fields in Optoelectronics, Prentice-Hall Series in Solid State Physical Electronics* (Prentice Hall, Incorporated, Englewood Cliffs, NJ, 1984).

[34] D. R. Rowland and J. D. Love, Evanescent wave coupling of whispering gallery modes of a dielectric cylinder, IEE Proc. J Optoelectron. **140**, 177 (1993).

[35] A. Yariv, Universal relations for coupling of optical power between microresonators and dielectric waveguides, Electron. Lett. **36**, 321 (2000).

[36] A. Yariv, Coupled-mode theory for guided-wave optics, IEEE J. Quantum Electron. **9**, 919 (1973).

[37] V. R. Almeida, R. R. Panepucci, and M. Lipson, Nanotaper for compact mode conversion, Opt. Lett. **28**, 1302 (2003).

[38] C. Xiong, X. Zhang, A. Mahendra, J. He, D.-Y. Choi, C. J. Chae, D. Marpaung, A. Leinse, R. G. Heideman, M. Hoekman, C. G. H. Roeloffzen, R. M. Oldenbeuving, P. W. L. van Dijk, C. Taddei, P. H. W. Leong, and B. J. Eggleton, Compact and reconfigurable silicon nitride time-bin entanglement circuit, Optica **2**, 724 (2015).

[39] M. H. P. Pfeiffer, A. Kordts, V. Brasch, M. Zervas, M. Geiselmann, J. D. Jost, and T. J. Kippenberg, Photonic Damascene process for integrated high-Q microresonator based nonlinear photonics, Optica **3**, 20 (2016).

[40] P. Del'Haye, O. Arcizet, M. L. Gorodetsky, R. Holzwarth, and T. J. Kippenberg, Frequency comb assisted diode laser spectroscopy for measurement of microcavity dispersion, Nat. Photonics **3**, 529 (2009).

[41] M. L. Gorodetsky, A. D. Pryamikov, and V. S. Ilchenko, Rayleigh scattering in high-Q microspheres, J. Opt. Soc. Am. B **17**, 1051 (2000).

[42] A. Taflove and S. C. Hagness, Computational Electrodynamics: The Finite-Difference Time-Domain Method,

Artech House Antennas and Propagation Library (Artech House, Norwood, MA, 2005).

[43] J.-P. Berenger, *Perfectly Matched Layer (PML) for Computational Electromagnetics* (Morgan & Claypool, 2007).

[44] W. W. Lui, T. Hirono, K. Yokoyama, and W.-P. Huang, Polarization rotation in semiconductor bending waveguides: A coupled-mode theory formulation, J. Lightwave Technol. **16**, 929 (1998).

[45] L. Liu, Y. Ding, K. Yvind, and J. M. Hvam, Efficient and compact TE–TM polarization converter built on silicon-on-insulator platform with a simple fabrication process, Opt. Lett. **36**, 1059 (2011).